PNAS RESEARCH ARTICLE | BIOPHYSICS AND COMPUTATIONAL BIOLOGY

Transmembrane proteins tetraspanin 4 and CD9 sense membrane curvature

Raviv Dharan[a,b], Shahar Goren[a,b,c], Sudheer Kumar Cheppali[a,b], Petr Shendrik[a], Guy Brand[a], Alisa Vaknin[a], Li Yu[d], Michael M. Kozlov[b,e], and Raya Sorkin[a,b,1]

Edited by James Hurley, University of California, Berkeley, CA; received June 2, 2022; accepted September 26, 2022

Multiple membrane-shaping and remodeling processes are associated with tetraspanin proteins by yet unknown mechanisms. Tetraspanins constitute a family of proteins with four transmembrane domains present in every cell type. Prominent examples are tetraspanin4 and CD9, which are required for the fundamental cellular processes of migrasome formation and fertilization, respectively. These proteins are enriched in curved membrane structures, such as cellular retraction fibers and oocyte microvilli. The factors driving this enrichment are, however, unknown. Here, we revealed that tetraspanin4 and CD9 are curvature sensors with a preference for positive membrane curvature. To this end, we used a biomimetic system emulating membranes of cell retraction fibers and oocyte microvilli by membrane tubes pulled out of giant plasma membrane vesicles with controllable membrane tension and curvature. We developed a simple thermodynamic model for the partitioning of curvature sensors between flat and tubular membranes, which allowed us to estimate the individual intrinsic curvatures of the two proteins. Overall, our findings illuminate the process of migrasome formation and oocyte microvilli shaping and provide insight into the role of tetraspanin proteins in membrane remodeling processes.

membrane curvature | migrasomes | optical tweezers | tetraspanin

Significance

Various physiological processes involve protein-driven shaping and remodeling of membranes. Uncovering the mechanisms leading to membrane remodeling is therefore essential for understanding biological processes such as fertilization, as well as to allow intervention in such processes when needed. Multiple membrane remodeling processes are associated with proteins from the tetraspanin family by yet unknown mechanisms. In particular, tetraspanin4 promotes formation of cellular organelles called migrasomes, which mediate cell–cell communication, and CD9 is indispensable for the process of fertilization. Here, we found that these proteins are curvature sensors with a preference for positive membrane curvature. As the transmembrane region of tetraspanins is highly conserved, the entire tetraspanin family may sense membrane curvature and, by this, mediate tetraspanin functions.

Tetraspanins (TSPANs) are small proteins with four transmembrane domains present in every cell type (1, 2). TSPANs regulate cell morphology, adhesion, motility, fusion, and signaling in diverse organs (3). The functionality of TSPANs is thought to be dependent on their ability to form a distinct class of membrane domains by association among themselves and with other integral proteins and adhesion molecules (1, 4). TSPAN domains are dynamic and can change their composition and organization between different cell lines and cell states (5).

Prominent members of the TSPAN family are tetraspanin 4 (TSPAN4) and CD9, whose crucial intracellular functions have been newly revealed. TSPAN4 has been shown to regulate formation of migrasomes, the recently discovered cell organelles playing essential roles in cell-cell signaling, lateral transfer of messenger RNA and proteins, transport of damaged mitochondria, and organ morphogenesis in vivo (6–9). Structurally, migrasomes are few microns large spherical swellings formed on retraction fibers. Retraction fibers are tens of microns long and about 100-nanometer-thick protrusions of cell plasma membrane pulled out of the cell rear during migration (10). Recent evidence suggests that retraction fibers are enriched with TSPANs, and overexpression of 14 different TSPANs enhances migrasome formation (6). Among them, TSPAN4 is one of the most effective. In the initial stage of migrasome biogenesis, migrasomes have a relatively low TSPAN4 concentration. In the migrasome growing stage, however, TSPAN4 concentration in the migrasome membrane increases with time and was found to be essential for the mature migrasome's stabilization (11).

CD9 is involved in the viral infection cycle and is localized to the growing tips of viral buds (12). Furthermore, CD9 is imperative for the process of fertilization. Knockout of the CD9 gene resulted in abnormal distribution and shapes of microvilli in oocytes, which severely damaged female fertility (13–15).

While the biological roles of TSPAN4 and CD9 have been intensively addressed, the physicochemical mechanisms underlying their functioning in cells remain unknown. Specifically, the physical forces underlying the observed affinity of these proteins to the strongly curved membranes of the retraction fibers (for TSPAN4) and microvilli (for CD9) have never been explored. At the same time, the existing structural data suggest that the background for this affinity may be related to sensing by these proteins of the membrane curvature. According to a recent crystallographic study (16), CD9 has an asymmetric cone-like effective molecular shape and hence a positive intrinsic curvature (17–19). As the transmembrane region is highly conserved for all TSPANs (15), this

Author contributions: R.D., A.V., M.M.K., and R.S. designed research; R.D., S.G., S.K.C., P.S., M.M.K., and R.S. performed research; L.Y. contributed new reagents/analytic tools; R.D., S.G., and G.B. analyzed data; and R.D., M.M.K., and R.S. wrote the paper.

The authors declare no competing interest.

This article is a PNAS Direct Submission.

[1]To whom correspondence may be addressed. Email: rsorkin@tauex.tau.ac.il.

This article contains supporting information online at http://www.pnas.org/lookup/suppl/doi:10.1073/pnas.2208993119/-/DCSupplemental.

Published October 17, 2022.

whole family of proteins, including TSPAN4, might be characterized by considerable molecular intrinsic curvatures, which can provide a background for membrane curvature generation and sensing by these proteins in various processes (20–24).

Here, we revealed and quantitatively substantiated that TSPAN4 and CD9 are membrane curvature sensors. We experimentally demonstrated the large affinity of these proteins to membrane tubes having a high positive curvature. We derived a thermodynamic model for protein enrichment in membrane tubes, which successfully described the strong partitioning of these proteins between nearly flat membranes of giant plasma membrane vesicles (GPMVs) and the strongly curved membrane tubules. Combining the experimental results and the modeling, we estimated the effective intrinsic curvatures of TSPAN4 and CD9.

Results

We designed an artificial system of membrane tubules mimicking the cell retraction fibers and the shapes of oocytes-microvilli. TSPAN4 or CD9 with a green fluorescent protein (GFP) reporter attached to the C terminus of TSPAN proteins was transiently expressed in HEK293T cells (Fig. 1*A*; see *Materials and Methods* for details). GPMVs with TSPAN4 or CD9 in their membrane were immobilized on a glass surface within a custom-made chamber mounted on the stage of a correlated optical tweezers–confocal fluorescence microscope (Fig. 1 *A* and *B*). An optically trapped polystyrene bead was pushed toward an immobilized GPMV, and a membrane nanotube was pulled out of the vesicle (Fig. 1*C*). The nanotube radius was significantly smaller—and hence the curvature was considerably larger—than those of the effectively planar GPMVs. Measurement of protein partitioning between the GPMV and the tubule allowed us to investigate the curvature sensing by TSPAN4 and CD9. After the tube was pulled, we monitored the fluorescence of the GPMV and the tube (Fig. 1*C*). The fluorescence intensity of both TSPAN4-GFP and CD9-GFP at the membrane tube was significantly higher than that at the flat membrane, indicating that the proteins prefer higher membrane curvature (Fig. 1*C* and *SI Appendix*, Fig. S1*A*). This increase occurred immediately upon pulling a tether and remained stable for a given tension upon tube elongation (*SI Appendix*, Fig. S2).

Hence, membrane curvature can induce TSPAN4 and CD9 redistribution from the flat membrane of a GPMV to the curved tubular membrane. In order to quantify this effect, we labeled the membranes with a plasma membrane dye (DiI-C12 or Deep red) by incubating the cells with the dye before generating GPMVs (Fig. 1*D* and *SI Appendix*, Fig. S1*B*). Protein enrichment could be measured by comparing its fluorescence intensity to that of the membrane dye (22, 25). If the affinity of TSPAN4-GFP\CD9-GFP to the tube is higher than to the flat membrane, the tube will appear green compared to the vesicle. On the other hand, if the affinity to the tube is the same or lower than to the flat membrane, the tube will have the same color as the vesicle or will appear redder (DiI-C12 or Deep red).

To quantify protein redistribution to the curved membrane, we defined the sorting ratio, S, as

$$S = \frac{\left(I_{TSPAN-GFP}/I_{membrane\ dye}\right)_{tube}}{\left(I_{TSPAN-GFP}/I_{membrane\ dye}\right)_{vesicle}}, \quad [1]$$

where I is the fluorescence intensity of the relevant component. According to this definition, a value of S greater than 1 indicates that the tube is enriched in TSPAN4\CD9. Our data showed that for both TSPAN4 and CD9, the sorting ratio was much higher than 1 (Fig. 1*E* and *SI Appendix*, Fig. S2), demonstrating the striking sensitivity of these proteins to membrane curvature. A control experiment was performed with the transmembrane protein ACE2-GFP, which did not partition into the tube (Fig. 1*E* and *SI Appendix*, Fig. S1*C*). These high sorting ratios demonstrate that TSPAN4 and CD9 sense membrane curvature and partition into membranes with high positive curvature. The range of sorting ratios measured for TSPAN4 and CD9 was broad, ranging between 1.5 and 10. A possible cause for this is

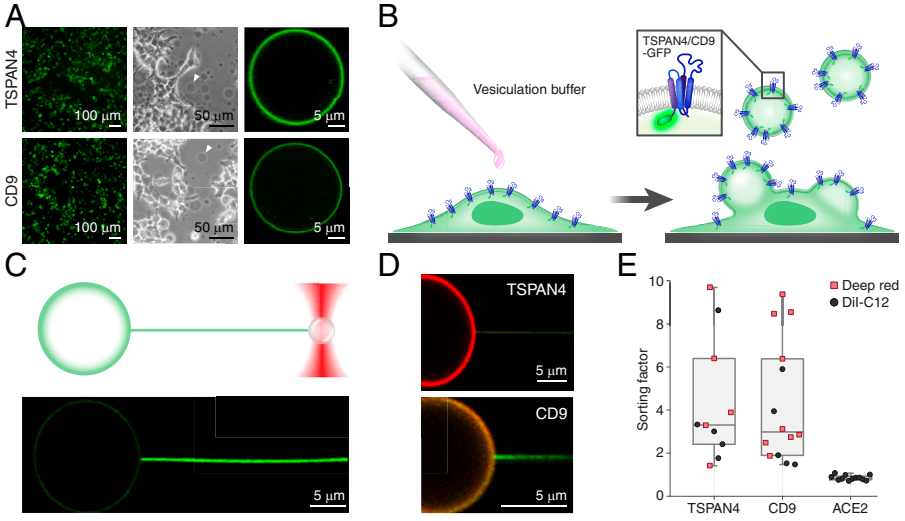

Fig. 1. TSPAN4 and CD9 partitioning into curved membranes. (*A*) Microscopy images of HEK293T cells expressing TSPAN4\CD9-GFP (*Left Images*). After treatment with a vesiculation buffer, GPMVs can be seen floating in the sample or attached to the cells (*Middle Images*, representative GPMVs indicated by white arrowheads). The isolated GPMVs contained TSPAN4\CD9-GFP in their membrane (*Right Images*). (*B*) Illustration of the experimental procedure of GPMV formation. (*C*) Confocal microscopy image of a membrane tube pulled out of a GPMV containing TSPAN4-GFP. *Top*: Schematic illustration of the tube-pulling experiment. *Bottom*: The tube was highly enriched with TSPAN4-GFP compared to the vesicle. (*D*) Confocal microscopy images of a tube pulled from GPMVs containing TSPN4-GFP (*Top*) or CD9-GFP (*Bottom*) and labeled with the membrane dye DiI-C12 (GFP-green, DiI-C12–red). (*E*) Box plot comparing the sorting ratio of TSPAN4-GFP (n = 10 vesicles), CD9-GFP (n = 14 vesicles), and ACE2-GFP (control, n = 12 vesicles). Black circles and red squares represent experiments conducted with DiI-C12 and Deep red, respectively. Box-whisker plot horizontal lines represent (from the top) the maximum, the third quartile, the median, the first quartile and the minimum.

the variability of the tube curvature, as in this assay tube curvature was not controlled.

In order to confirm our hypothesis, we demonstrated that higher membrane curvatures induce higher TSPAN4\CD9 sorting. For this purpose, we integrated micropipette aspiration within dual-trap-tweezers confocal fluorescence microscopy. The combination of micropipette aspiration with optical trapping allows one to control the membrane tension of the vesicle and thus the diameter of the membrane tube (i.e., the membrane curvature of the tube) while measuring the pulling force of the tube (Fig. 2 *A* and *B*). We generated tensions in the vesicle membrane in the range of $1.1 \times 10^{-5} - 1.3 \times 10^{-4}\ N/m$. First, we pulled the tube at a relatively low membrane tension, which resulted in a partitioning of TSPAN4\CD9 into the tube (Fig. 2*C*). We then increased the tension in the vesicle, which led to a higher pulling force (*SI Appendix*, Fig. S3) and concomitantly to higher tube curvature. This resulted in further protein enrichment in the tube (Fig. 2*C*).

To understand the physical factors determining protein sorting in our system, we developed a thermodynamic model (*SI Appendix*). We assumed the membrane monolayers were composed of lipid matrix with vanishing spontaneous curvature and embedded inclusions characterized by a positive molecular intrinsic curvature. We considered the system to consist of a flat membrane subjected to a constant tension and a tube (membrane tether) pulled out of the flat membrane by application of a local force. The model accounted for interplay between the bending energy of the membrane tube, the energy of the tension, and the entropy of the protein distribution in the membrane plane. Minimization of system free energy enabled us to predict the dependence of the tube equilibrium radius, the pulling force, and the difference between the protein concentrations in the tubular and flat membrane regions on the protein intrinsic curvature and the tension (*SI Appendix*). The free energy landscapes and model predications for different values of the model parameters are shown in *SI Appendix*, Figs. S4 and S5.

We next set out to fit our experimental results to the model predictions. This was done by numerically solving the model equations for various values of the membrane's bending rigidity, κ, and the protein's intrinsic curvature, ζ, with a goal of finding the values of these two parameters providing the best agreement between the predicted and the experimentally determined values of the pulling force and sorting ratio as functions of the tension for each GPMV. The used parameters were the protein's initial surface fraction (TSPAN4: 0.057 to 0.636%; CD9: 0.033 to 0.292%) and the in-plane areas of a lipid molecule and an inclusion taken as 0.7 nm^2 (26) and 9.6 nm^2, respectively, the latter based on the crystal structure of CD9 (16).

In most cases, the model predictions were in a good agreement with the measured values of the force and the sorting ratio (Fig. 3 *A* and *B*); yet, for some of the experiments, there were substantial deviations of the predicted values from the measured ones (*SI Appendix*, Figs. S6 and S7). The fitting resulted in mean values of the molecular intrinsic curvature of $0.11 \pm 0.03\ nm^{-1}$ for TSPAN4 and $0.12 \pm 0.03\ nm^{-1}$ for CD9 (*SI Appendix*, Tables S1 and S2).

The model predicted sorting ratio would monotonically increase with increasing tension or equivalently decreasing tube radius. This trend for sorting as a function of the tether radius was observed experimentally for both TSPAN4 and CD9 (Fig. 3*B*). Theoretically, the sorting ratio dependence on the protein concentration in

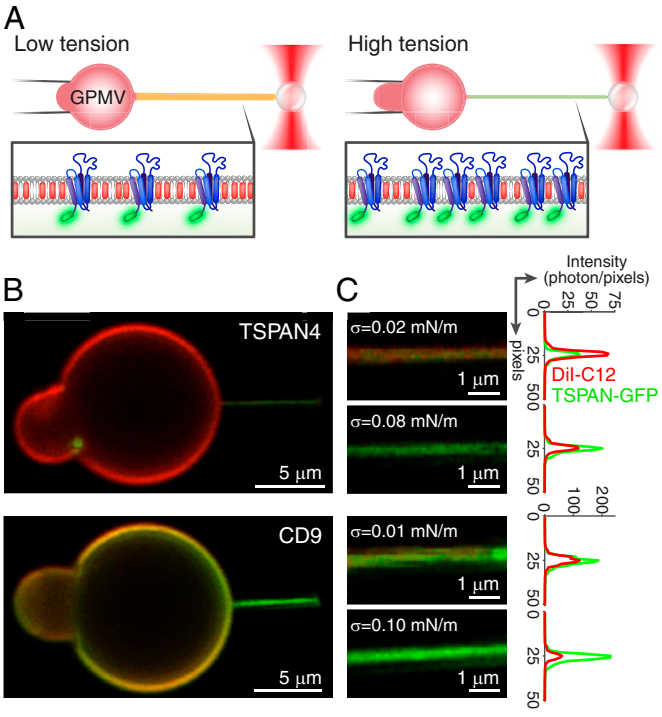

Fig. 2. Higher membrane curvature increases TSPAN4 and CD9 sorting. (*A*) Schematic illustration of tube pulling with a controllable membrane tension setup. An optically trapped bead is used to pull a membrane tube from an aspirated GPMV by a micropipette. The pressure in the pipette determines the membrane tension and hence controls the tube radius. In parallel, the pulling force is measured while the GPMV and tube are scanned by confocal fluorescence microscopy and monitored in real time by bright-field microscopy. TSPAN molecules are in blue with green GFP, red rectangles correspond to DiI molecules. (*B*) Confocal microscopy images of aspirated GPMVs containing TSPAN4-GFP or CD9-GFP (green) and labeled with DiI-C12 (red). (*C*) Confocal microscopy images of membrane tubes pulled from the GPMVs shown in *B* at relatively low and high membrane tension, as indicated. *Right*: The normalized intensity profiles of GFP and DiI-C12 of each image are presented.

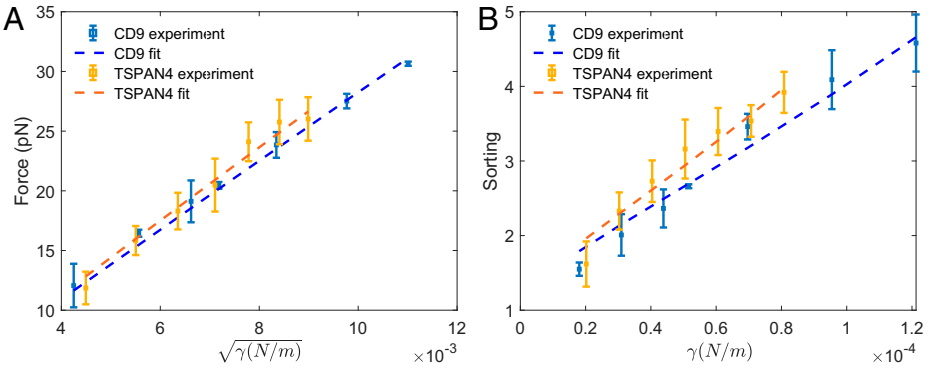

Fig. 3. Free energy model for protein enrichment in membrane tube. (*A* and *B*) Plots for the pulling force as a function of the square root of membrane tension (*A*) and sorting ratios as a function of the membrane tension (*B*) of representative GPMVs containing TSPAN4-GFP or CD9-GFP. Squares are the mean force values; error bars are SD. Dashed lines are fits of the numerical solutions for the free energy model with bending moduli $\kappa = 32.935 \pm 1.774\ k_BT$ and intrinsic curvature $\zeta = 0.120 \pm 0.006\ nm^{-1}$ for TSPAN4 and for CD9: $\kappa = 27.685 \pm 0.988\ k_BT$ and $\zeta = 0.121 \pm 0.007\ nm^{-1}$.

the flat membrane playing the role of a protein reservoir was predicted to be weak (*SI Appendix*, Fig. S5 *H* and *J*). The experimental data of the sorting ratio dependency on protein concentration for TSPAN4 and CD9-GFP did not show a conclusive trend (*SI Appendix*, Fig. S8).

The results described above correspond to the experiments in which flat membrane tension gradually increased from low to high values. For tubes, which did not rupture in the course of the tension increase, we investigated the evolution of the sorting ratio during a gradual decrease in the tension back to low values. On this backtrack, the sorting ratios were higher than those corresponding to the same values of growing tension. Hence, sorting exhibited hysteresis, which was stronger for TSPAN4 than for CD9 (Fig. 4 *A*–*F*). We hypothesized that this hysteresis is a result of an attractive interaction between TSPAN proteins leading to domain formation, which differs between TSPAN4 and CD9 due to differences in their extracellular loops mediating the interaction. Based on the determined structure of CD9 (16) and the predicted structure of TSPAN4 (27, 28), TSPAN4 has a larger extracellular part compared to CD9, potentially leading to more pronounced protein–protein interactions and hence a stronger hysteresis.

In order to test this, we designed an experiment where the extracellular parts of TSPAN4 proteins in GPMVs were removed by proteolytic cleavage with proteinase K (Fig. 4 *G*–*I* and *SI Appendix*, Fig. S9), a serine protease that digests the extracellular region of transmembrane proteins (29, 30). We found that the hysteresis of TSPAN4 was abolished upon this treatment.

Discussion

TSPAN proteins are ubiquitous in all cell types and are involved in diverse cellular phenomena (1, 2). Prominent examples are the critical role of TSPAN4 in the formation of migrasomes on retraction fibers (6) and the essential involvement of CD9 in fertilization that occurs at the microvilli membrane of egg cells (13–15). A common feature of the two processes is a preferential localization of TSPAN4 and CD9 to the strongly curved membranes of the retraction fibers and microvilli, respectively. The driving force leading to such localization remains unknown.

Here, we discovered that both CD9 and TSPAN4 are membrane curvature sensors. Using a biomimetic system of membrane tubules with controlled radii pulled out of nearly flat membranes of GPMVs, we demonstrated a preferential partitioning of TSPAN4 and CD9 into membrane regions of high positive curvature. To quantitatively characterize the curvature sensitivity of these proteins, we measured the protein enrichment in the tubules compared to the flat membranes as a function of membrane tension. Based on these results, we propose that the driving force for the retraction fibers and microvilli enrichment of TSPAN4 and CD9 is driven by membrane curvature. It is important to consider the fact that GPMVs are derived from natural cellular membranes and thus contain numerous membrane proteins in addition to the proteins of interest. Thus, there could be a potential scenario wherein TSPAN proteins do not sense curvature by themselves but rather are recruited to the tubular membranes by other curvature-sensing proteins. To address this question, we devised an experiment where we significantly reduced TSPAN interactions with other proteins. To this end, we "shaved off" the extracellular domains of transmembrane proteins using an accepted procedure that is commonly used for this purpose (29, 30). Following this treatment of TSPAN4-containing GPMVs, we still observed similarly high sorting values of TSPAN redistribution into the membrane tethers (Fig. 4 *G*–*I*), demonstrating that curvature sensitivity is an intrinsic property of TSPAN4 rather than a result of recruitment by other proteins and that this property is uniquely attributed to the transmembrane part of the protein, which is expected to have a conical shape based on Alphafold prediction (27, 28), similar to the molecular shape determined for CD9 (16). Importantly, we also observed abolishment by this treatment of the hysteresis of TSPAN4 redistribution between the tether and the GPMV membranes (Fig. 4 *G*–*I*), which validates the efficiency of the shaving procedure.

To substantiate our proposal that the driving force for retraction fibers and microvilli enrichment in TSPAN4 and CD9 is membrane curvature, we developed a simple thermodynamic model for protein partitioning between a flat membrane reservoir subject to lateral tension and a tubular membrane pulled out of the reservoir by application of a local force. The model accounted only for the interplay between the membrane curvature and the intrinsic curvature of the proteins and did not consider any protein–protein interactions. While the model was able to recover the sorting ratio measured in most of the experiments, in a number of cases there were notable differences between the theoretical predictions and the experimental data. One main difference was observed for the experiments in which the flat membrane was subject to high tensions, and as a result, the tubular membrane reached large curvature values. In the large tension range, the measured sorting ratios usually reached a plateau as a function of the tension, whereas the model

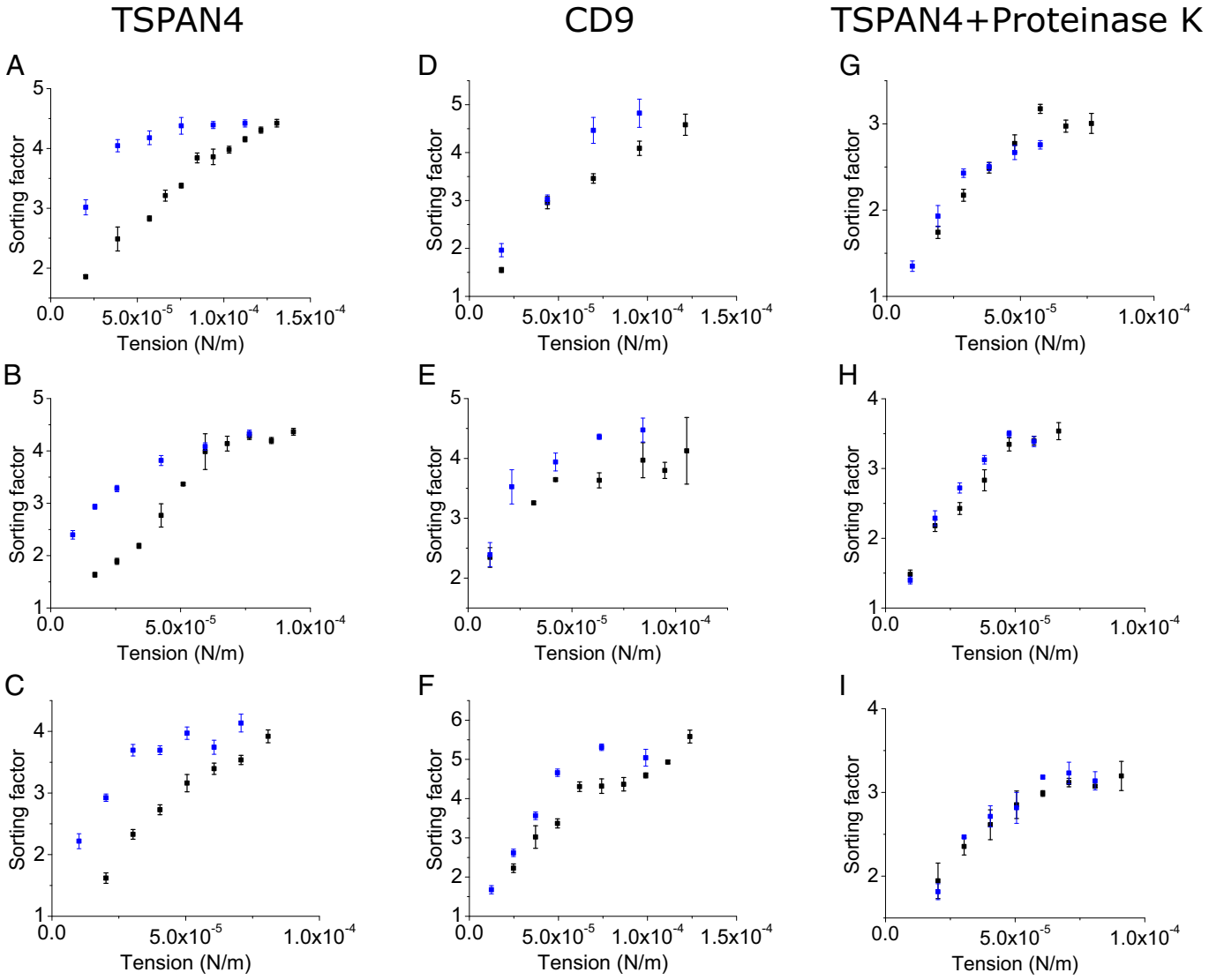

Fig. 4. Sorting hysteresis of TSPAN4 and CD9. (*A–F*) Membrane tubes were pulled from aspirated GPMVs, which contained TSPAN4-GFP (*A–C*) or CD9-GFP (*D–F*) and the membrane dye DiI-C12, at relatively low tension. Next, by increasing the aspiration pressure, membrane tension was increased. This resulted in higher TSPAN-GFP tube enrichment (i.e., higher sorting ratio). When the aspiration pressure was reduced, the sorting ratios were higher for the same membrane tension values. Black squares represent tension increase, whereas blue squares represent tension decrease. Error bars are SEM. (*G–I*) GPMVs with TSPAN4-GFP and DiI-C12 were incubated with 20 μg/mL proteinase K at 37 °C for 45 min prior to the experiment. This treatment abolished the sorting ratio hysteresis.

predicted a continuing increase in the sorting ratio. Furthermore, while the model did not predict any hysteresis of the protein sorting ratio, for TSPAN4 the sorting ratios measured for gradual increase on tension were considerably lower than those observed during the tension decrease for the same tension values. For CD9, the observed hysteresis was mild.

All these differences between the observations and the theoretical predictions can be explained by interactions between TSPAN molecules, which were previously described for TSPANs (1–5), and are likely mediated by the large extracellular loop of TSPAN proteins (31). According to our results, these protein–protein lateral interactions are stronger for TSPAN4 than for CD9. The hypothesis that the inter-TSPAN interaction is the driving force behind the observed phenomena, which are not accounted for by the present model, is supported by the detected effects of removal of the extracellular parts of the GPMV transmembrane proteins by proteinase K, which abolished the hysteresis of TSPAN4 sorting.

While our simple model does not account for interactions between the TSPAN molecules, it nonetheless effectively explains the high sorting ratios of TSPAN4 and CD9 and their dependence on tension in most of the tension range. Importantly, it allowed us to estimate the effective molecular intrinsic curvatures of the two proteins. The obtained high values of these intrinsic curvatures illuminate the strong influence of membrane shape on the localization and enrichment of TSPAN4 and CD9.

Materials and Methods

Cell Culture, TSPAN4-GFP, CD9-GFP, and ACE-GFP Expression Plasmids, Cell Transfection, and GPMV Isolation. HEK293T cells were cultured at 37 °C and 5% CO_2 in Dulbecco's modified Eagle's medium (Gibco, Thermo Fisher scientific) supplemented with 10% fetal bovine serum (Biological industries) and 1% penicillin-streptomycin (Gibco, Thermo Fisher scientific).

Complementary DNAs of mouse-TSPAN4, human-CD9, or human-ACE2 were cloned into pEGFP-N_1. HEK293T cells were plated in 25-cm^2 flasks coated with poly-L-lysine (Sigma-Aldrich) to keep the cells attached during the blebbing process and to minimize cell debris in the solution. At 50% confluency, cells were transiently transfected with 5 μg DNA using Lipofectamine 2000 (Invitrogen) according to the manufacture's protocols and then grown for 24 to 36 h for protein expression. GPMVs were produced according to a published protocol (32).

Briefly, following TSPAN4\CD9\ACE2–GFP expression, the cells were stained with DiI-C12 (Invitrogen) or CellMask Deep red (Invitrogen) membrane dye, washed with GPMV buffer (20 mM 4-(2-hydroxyethyl)-1-piperazineethanesulfonic acid [HEPES], 150 mM NaCl, and 2 mM $CaCl_2$, pH 7.4) twice and incubated with 1 mL GPMV buffer containing 1.9 mM dithiothreitol (Sigma-Aldrich) and 27.6 mM formaldehyde (Sigma-Aldrich). Secreted GPMVs were then collected and isolated from the cells and immediately used for the optical trapping experiments.

Giant Unilamellar Vesicle (GUV) Preparation. Chloroform stock solutions of 99.9% 1,2-dioleoyl-sn-glycero-3-phosphocholine (Avanti Polar Lipids) and 0.1% Oregon green 488 1,2-dihexadecanoyl-sn-glycero-3-phosphoethanolamine (Oregon green 488 DHPE; Invitrogen) were mixed at a final lipid concentration of 0.25 mM. GUVs were grown on indium tin oxide coated glass slides (Nanion Technologies). Then, 40 μL 0.25 mM lipid solution in chloroform was gently spread with a needle on the slide, dried under argon gas, and placed in a vacuum overnight. GUVs were then grown by electroformation in 275 mL 200 mM sucrose solution, using a Vesicle Prep Pro instrument (Nanion Technologies). The electroformation voltage was increased stepwise to 3 V (5 Hz) and applied at 37 °C for 2 h.

Tube Pulling from Immobilized GPMVs. The experiments were performed using a C-Trap confocal fluorescence optical tweezers setup (Lumicks) made of an inverted microscope based on a water-immersion objective (numerical aperture, 1.2) together with a condenser top lens placed above the flow cell. The optical traps were generated by splitting a 10W 1,064-nm laser into two orthogonally polarized, independently steerable optical traps. To steer the two traps, one coarse-positioning piezo stepper mirror and one accurate piezo mirror were used. Optical traps were used to capture polystyrene microbeads. The displacement of the trapped beads from the center of the trap was measured and converted into a force signal by back-focal plane interferometry of the condenser lens using two position-sensitive detectors. The samples were illuminated by a bright-field 850-nm light-emitting diode and imaged in transmission onto a metal-oxide semiconductor (CMOS) camera.

Confocal Fluorescence Microscopy. The C-Trap uses a three-color, fiber-coupled laser with wavelengths of 488, 561, and 638 nm for fluorescence excitation. Scanning was done using a fast tip/tilt piezo mirror. For confocal detection, the emitted fluorescence was descanned, separated from the excitation by a dichroic mirror, and filtered using an emission filter (Blue: 500 to 550 nm, Green: 575 to 625 nm, and Red: 650 to 750 nm). Photons were counted using fiber-coupled single-photon counting modules. The multimode fibers served as pinholes providing background rejection.

Experimental Chamber. Polydimethylsiloxane walls were placed on the bottom coverslip (Bar Naor) coated with poly-L-lysine (Sigma-Aldrich) and mounted onto an automated XY-stage. The GPMVs sample was added to the chamber, and after about 15 min, a few drops of oil were put on the sample surface to prevent evaporation. In order to pull a membrane tube, an optically trapped polystyrene bead (3.43 μm; Spherotech) was brought in contact with the GPMV for about a minute and then moved away from the vesicle. For confocal imaging, the 488-, 561-, and 638-nm lasers were used for GFP, DiI-C12, and Deep red excitation, respectively, with emission detected in three channels (Blue, Green, and Red).

Tube Pulling from Aspirated GPMVs. A micropipette aspiration setup including a micromanipulator (Sensapex) holding a micropipette with a diameter of 5 μm (Biological Industries) connected to a Fluigent EZ-25 pump was integrated with our optical tweezers instrument. Before and after each experiment, zero-suction pressure was found by aspirating a polystyrene bead into the pipette and reducing the suction pressure until the bead stopped moving. A membrane tube was pulled from aspirated GPMVs using beads trapped by the optical tweezers. First, a membrane tube was pulled at relatively low suction pressure (0.05 to 0.1 mbar, corresponding to 1 to 2×10^{-5} N/m membrane tension); then we gradually increased the suction pressure (usually by 0.05 to 0.1 mbar) until we reached values in the range of 0.3 to 0.7 mbar (corresponding to 5 to 13×10^{-5} N/m membrane tension), and then we gradually released back the pressure until reaching zero pressure. At each suction pressure, we monitored the force for at least 1 min and scanned at least three confocal fluorescence scans (unless the tube was ruptured). For confocal imaging, the 488-nm and 561-nm lasers were used for GFP and DiI-C12 excitation, with emission detected in two channels (Blue, Green). In some experiments (Fig. 4 *G–I*), the GPMVs were incubated before the tube pulling assay with 20 μg/mL proteinase k (QIAGEN) at 37 °C for 45 min. The reaction was quenched with 2 mM phenylmethylsulfonyl fluoride (Acros Organics) in dimethyl sulfoxide, and the GPMVs were immediately used.

Direct in-Gel Fluorescence. For in-gel fluorescence analysis (33, 34), the GPMVs were centrifuged (40,000 × *g*, 45 min at 4 °C), and the pellet was resuspended with 100 μL GPMV buffer supplemented with 1% (wt/vol) of *n*-Dodecyl β-D-maltoside (Anatrace). Next, the suspension was incubated on a rotating device for 1 h at 4 °C. Subsequently, the mixture was cleared by centrifugation for 10 min at 20,000 × *g*. The cleared supernatant was supplemented with Laemmli sample buffer, followed by 10 min of incubation at room temperature. Finally, the product was analyzed by 16% Tris-Glycine gel electrophoresis, and the fluorescence was detected using the Fusion FX7 imager.

Data Analysis. Data acquisition was carried out using Bluelake, a commercial software from Lumicks. This software stores experimental data acquired during experiments with the C-Trap in HDF5 files, which can be processed using Lumicks' Pylake python package. Images of the confocal scans were reconstituted from photon count per pixel data in the HDF5 files using Pylake. All data analysis was performed with custom-written Python scripts. Fluorescence intensity profiles were obtained from the images by averaging the photon count of the relevant fluorescent channel in the region of interest. Code used for data analysis and model fitting is available at https://gitlab.com/raviv_dharan/protein-curvature-sensitivity-analysis.

GPMV Protein Density. The GPMV protein–GFP density was determined based on published protocols (35, 36). Briefly, the fluorescence intensity of each GPMV was quantified according to the blue channel photon count of the confocal image in the region of interest. In separate experiments, GUVs containing 0.1% Oregon green DHPE were imaged, which provided a reference signal of known fluorophore concentration in the membrane. One hundred immobilized GUVs were scanned at the same confocal setup, and the fluorescence intensity of the GUV was related to the fluorophore density using the equation $x_{GUV}^{Oregon-DHPE} = C_{protocol} \times I_{GUV}^{Oregon-DHPE}$, where x is the mole fraction of the fluorophore in the GUV, $C_{protocol}$ depends on the confocal setup parameters and the fluorescence yield of the fluorophore, and I is the fluorescence intensity of the fluorophore. To compensate for the difference in the fluorescence intensity yield between Oregon green and GFP, the fluorescence intensity of water-solvated Oregon green and GFP was measured (*SI Appendix*, Fig. S10). The mole fraction of the protein in the GPMV was calculated by the equation

$$x_{GPMV}^{Protein-GFP} = C_{protocol} \times \frac{I_{GPMV}^{Protein-GFP}}{I_{Soluble}^{GFP} / I_{Soluble}^{Oregon-DHPE}}.$$

Data, Materials, and Software Availability. Raw data have been deposited in the OSF (https://osf.io/p47c8/?view_only=963a1c0c7a744eb8b7e57daf98e23d07) (37).

ACKNOWLEDGMENTS. R.S. acknowledges support by the Israel Science Foundation (Grant No. 1289/20). S.K.C. acknowledges support by the Ratner Center for Single Molecule Science. M.M.K. was supported by Deutsche Forschungsgemeinschaft through SFB 958 "Scaffolding of Membranes" and Israel Science Foundation Grant No. 3292/19 and holds the Joseph Klafter Chair in Biophysics.

Author affiliations: [a]School of Chemistry, Raymond & Beverly Sackler Faculty of Exact Sciences, Tel Aviv University, 69978 Tel Aviv, Israel; [b]Center for Physics and Chemistry of Living Systems, Tel Aviv University, 69978 Tel Aviv, Israel; [c]School of Mechanical Engineering, The Iby and Aladar Fleischman Faculty of Engineering, Tel Aviv University, 69978 Tel Aviv, Israel; [d]The State Key Laboratory of Membrane Biology, Tsinghua University-Peking University Joint Centre for Life Sciences, Beijing Frontier Research Center for Biological Structure, School of Life Sciences, Tsinghua University, Beijing 100084, China; and [e]Department of Physiology and Pharmacology, Sackler Faculty of Medicine, Tel Aviv University, 69978 Tel Aviv, Israel

1. S. Charrin *et al.*, Lateral organization of membrane proteins : Tetraspanins spin their web. *Biochem. J.* **420**, 133–154 (2009).
2. M. Yáñez-Mó, O. Barreiro, M. Gordon-Alonso, M. Sala-Valdés, F. Sánchez-Madrid, Tetraspanin-enriched microdomains: A functional unit in cell plasma membranes. *Trends Cell Biol.* **19**, 434–446 (2009).
3. M. E. Hemler, Tetraspanin functions and associated microdomains. *Nat. Rev. Mol. Cell Biol.* **6**, 801–811 (2005).
4. R. L. Bailey *et al.*, The emerging role of tetraspanin microdomains on endothelial cells. *Biochem. Soc. Trans.* **39**, 1667–1673 (2011).
5. F. Le Naour, M. André, C. Boucheix, E. Rubinstein, Membrane microdomains and proteomics: Lessons from tetraspanin microdomains and comparison with lipid rafts. *Proteomics* **6**, 6447–6454 (2006).
6. Y. Huang *et al.*, Migrasome formation is mediated by assembly of micron-scale tetraspanin macrodomains. *Nat. Cell Biol.* **21**, 991–1002 (2019).
7. L. Ma *et al.*, Discovery of the migrasome, an organelle mediating release of cytoplasmic contents during cell migration. *Cell Res.* **25**, 24–38 (2015).
8. D. Jiang *et al.*, Migrasomes provide regional cues for organ morphogenesis during zebrafish gastrulation. *Nat. Cell Biol.* **21**, 966–977 (2019).
9. H. Jiao *et al.*, Mitocytosis, a migrasome-mediated mitochondrial quality-control process. *Cell* **184**, 2896–2910.e13 (2021).
10. C. Fan *et al.*, Cell migration orchestrates migrasome formation by shaping retraction fibers. *J. Cell Biol.* **221**, e202109168 (2022).
11. R. Dharan *et al.*, Tetraspanin 4 mediates migrasome formation via a two-stage mechanism. bioRxiv [Preprint] (2022). https://doi.org/10.1101/2022.07.11.499540. Accessed 11 July 2022.
12. S. Dahmane *et al.*, Nanoscale organization of tetraspanins during HIV-1 budding by correlative dSTORM/AFM. *Nanoscale* **11**, 6036–6044 (2019).
13. K. E. Runge *et al.*, Oocyte CD9 is enriched on the microvillar membrane and required for normal microvillar shape and distribution. *Dev. Biol.* **304**, 317–325 (2007).
14. K. Miyado *et al.*, Requirement of CD9 on the egg plasma membrane for fertilization. *Science* **287**, 321–324 (2000).
15. C. Boucheix, Severely reduced female fertility in CD9-deficient mice. *Science* **287**, 319–321 (2000).
16. R. Umeda *et al.*, Structural insights into tetraspanin CD9 function. *Nat. Commun.* **11**, 1606 (2020).
17. H. T. McMahon, J. L. Gallop, Membrane curvature and mechanisms of dynamic cell membrane remodelling. *Nature* **438**, 590–596 (2005).
18. H. T. McMahon, E. Boucrot, Membrane curvature at a glance. *J. Cell Sci.* **128**, 1065–1070 (2015).
19. A. Callan-Jones, P. Bassereau, Curvature-driven membrane lipid and protein distribution. *Curr. Opin. Solid State Mater. Sci.* **17**, 143–150 (2013).
20. N. Khattree, L. M. Ritter, A. F. X. Goldberg, Membrane curvature generation by a C-terminal amphipathic helix in peripherin-2/rds, a tetraspanin required for photoreceptor sensory cilium morphogenesis. *J. Cell Sci.* **126**, 4659–4670 (2013).
21. S. Aimon *et al.*, Membrane shape modulates transmembrane protein distribution. *Dev. Cell* **28**, 212–218 (2014).
22. E. Beltrán-Heredia *et al.*, Membrane curvature induces cardiolipin sorting. *Commun. Biol.* **2**, 225 (2019).
23. M. Simunovic, G. A. Voth, A. Callan-Jones, P. Bassereau, When physics takes over: BAR proteins and membrane curvature. *Trends Cell Biol.* **25**, 780–792 (2015).
24. P. Bassereau *et al.*, The 2018 biomembrane curvature and remodeling roadmap. *J. Phys. D Appl. Phys.* **51**, 343001 (2018).
25. G. Moreno-Pescador *et al.*, Curvature- and phase-induced protein sorting quantified in transfected cell-derived giant vesicles. *ACS Nano* **13**, 6689–6701 (2019).
26. N. Kučerka, S. Tristram-Nagle, J. F. Nagle, Structure of fully hydrated fluid phase lipid bilayers with monounsaturated chains. *J. Membr. Biol.* **208**, 193–202 (2005).
27. J. Jumper *et al.*, Highly accurate protein structure prediction with AlphaFold. *Nature* **596**, 583–589 (2021).
28. M. Varadi *et al.*, AlphaFold protein structure database: Massively expanding the structural coverage of protein-sequence space with high-accuracy models. *Nucleic Acids Res.* **50**, D439–D444 (2022).
29. A. Olaya-Abril, I. Jiménez-Munguía, L. Gómez-Gascón, M. J. Rodríguez-Ortega, Surfomics: Shaving live organisms for a fast proteomic identification of surface proteins. *J. Proteomics* **97**, 164–176 (2014).
30. M. I. Morandi *et al.*, Extracellular vesicle fusion visualized by cryo-EM. bioXriv [Preprint] (2022). https://doi.org/10.1101/2022.03.28.486013. Accessed 15 June 2022.
31. C. S. Stipp, T. V. Kolesnikova, M. E. Hemler, Functional domains in tetraspanin proteins. *Trends Biochem. Sci.* **28**, 106–112 (2003).
32. Z. Gerstle, R. Desai, S. L. Veatch, Giant plasma membrane vesicles: An experimental tool for probing the effects of drugs and other conditions on membrane domain stability. *Methods Enzymol.* **603**, 129–150 (2018).
33. D. Drew *et al.*, GFP-based optimization scheme for the overexpression and purification of eukaryotic membrane proteins in *Saccharomyces cerevisiae*. *Nat. Protoc.* **3**, 784–798 (2008).
34. P. M. Clark *et al.* Direct in-gel fluorescence detection and cellular imaging of *O*-GlcNAc-modified proteins. *J. Am. Chem. Soc.* **130**, 11576–11577 (2008).
35. S. Aimon *et al.*, Functional reconstitution of a voltage-gated potassium channel in giant unilamellar vesicles. *PLoS One* **6**, e25529 (2011).
36. J. Steinkühler *et al.*, Controlled division of cell-sized vesicles by low densities of membrane-bound proteins. *Nat. Commun.* **11**, 905 (2020).
37. R. Dharan *et al.*, Supplemental Data for "Transmembrane proteins tetraspanin 4 and CD9 sense membrane curvature." The Open Science Framework (OSF). https://osf.io/p47c8/?view_only=963a1c0c7a744eb8b7e57daf98e23d07. Deposited 16 July 2022.